Optical study of beyond EUV mask and mirrors

Naoki Hayase,[a] Tetsuo Harada[a]

[a] Center for EUV lithography, LASTI, University of Hyogo, NewSUBARU synchrotron radiation facility, Ako-gun Kamigori Kouto 1-1-2, Hyogo 678-1205, Japan

Abstract: Beyond EUV (BEUV) lithography at 6.6 nm wavelength suffers from the small refractive-index contrast and requires multilayer (ML) mirrors of around 200 pairs. The large number of ML interfaces amplifies scattered light arising from surface roughness, and a greater effective reflection plane depth (Z_{eff}) of ML drives mask 3D effect (M3D) in photomasks. **Background:** The problems originate from the same low-contrast constraint, and a systematic metric linking reactive surface growth and surface roughness has been lacking to improve reflectivity. In addition, nitride-based BEUV mask absorbers against M3D have not been optimized in our previous study. **Aim**: We investigate nitride-based BEUV optics to control kinetic roughness during gas-reactive deposition and identify a promising BEUV mask to control optical performance. **Approach**: A finite-mobility solid-on-solid model is introduced to describe reactive surface growth, in which chemisorption coverage governed by the Langmuir-Hinshelwood kinetics modifies the Ehrlich-Schwoebel (ES) and adatom diffusion barriers. As nitride-based components, we investigate TaN and CrN BEUV absorbers in terms of reflectivity, phase difference, and aerial images. **Results**: Our model predicts decreasing roughness with increasing chemisorption coverage, controlled by the ratio of the ES length to the adatom diffusion length. For photomask, CrN absorber gives 135° phase shifting at 62.6 nm thickness, at which the normalized image logarithmic slope (NILS) approaches saturation at 0.55 NA in our photomask model. **Conclusions**: Nitride interface kinetics suggests a route to roughness control for MLs and photomasks. CrN-based Att-PSMs are candidates for high-NA BEUV lithography at 0.55 NA with anamorphic (4x/8x) demagnification at an angle of incidence of around 6°.

Keywords: beyond EUV; multilayer; photomask; absorber; optical scattering; deposition; phase shift.

E-mail: hayase@lasti.u-hyogo.ac.jp

1 Introduction

Beyond EUV (BEUV) lithography at around 6.6 nm wavelength has been developed for the further downscaling of semiconductor devices [1,2]. BEUV optics require high-reflectance, high-durability multilayer (ML) mirrors for the design of exposure tools and photomasks. Surface roughness on mirrors causes a decrease in reflectivity with optical scattering. Minimization of surface roughness is necessary to reduce false defect detections in a mask inspection process and improve lithographic patterning [3].

The physical vapor deposition (PVD) process for MLs generally has two approaches: ion beam deposition (IBD) and magnetron sputtering (MS). The roughness of ML deposited by MS is greater than that of IBD, but MS is superior to IBD in terms of throughput for ML deposition in previous works [4,5]. Given an understanding of the deposition mechanism for roughness control, MS is expected to be a primary method for improving the productivity of mirrors and photomasks.

Table 1 shows the performance of EUV, BEUV, and Blue-X lithography, assuming that the Rayleigh coefficients are k_1 = 0.33 and k_2 = 1.0 for half-pitch (HP) resolution and depth-of-focus (DOF) [6]. After 0.75 NA EUV lithography, 0.55 NA BEUV is a candidate for 4 nm HP. In addition, a patterning error of reflection shadowing known as the mask 3D effect (M3D) is a concern, which originates from absorber thickness and effective reflection plane depth (Z_{eff}) of MLs [7]. BEUV ML exhibits a deeper Z_{eff} owing to the smaller difference of refractive index than EUV Mo/Si MLs, resulting in severe M3D and critical dimension (CD) variation at near-normal angles of incidence (AOI) [1]. Photomasks are mainly categorized into binary masks and attenuated phase shift masks (Att-PSMs) [8]. Binary masks rely on the extinction coefficient of materials to reduce reflectivity from ML. BEUV binary absorbers are predicted to require greater thickness than EUV masks, which amplifies M3D-induced CD errors and limits lithographic scalability. In contrast, Att-PSMs exploit controlled phase modulation and partial reflectivity to enhance image contrast. Att-PSMs are expected to allow thinner absorber designs compared with binary masks, by selecting suitable materials.

In this paper, we investigate a surface growth model of nitrogen gas reactive deposition in masks and mirrors for minimizing roughness. Furthermore, we propose a nitride-based Att-PSM structure for suppressing the M3D effect and identify the allowable NA and demagnification (DM) of exposures for high-NA BEUV lithography.

Table 1. Comparison of EUV, BEUV, and Blue-X lithography performance.

Title	Wavelength	NA	Resolution (HP)	DOF	Photomask
EUV	13.5 nm	0.33	13.5 nm	124.0 nm	Binary, Att-PSM
		0.55	8.1 nm	44.6 nm	Att-PSM
		0.75	5.9 nm	24.0 nm	
BEUV	6.6 nm	0.55	4.0 nm	21.8 nm	Undefined
		0.75	2.9 nm	11.7 nm	
Blue-X	3.1 nm	0.27	3.8 nm	42.5 nm	

2 Multilayer mirror

2.1 Surface Scattering

Surface roughness σ causes diffuse scattering, and total integrated scatter (TIS) represents the fraction of the total scatter and the specular reflection with AOI (θ_i) as given in Eq. (1) [9,10].

$$\mathrm{TIS}_N = 1 - \prod_{k=1}^{N} \exp\left[-\left(\frac{4\pi\sigma_k \cos\theta_{i,k}}{\lambda}\right)^2\right] \quad (1)$$

Fig. 1 shows the dependence of TIS on wavelength with the number of reflections, assuming the roughness from 0.1 nm to 0.4 nm with an AOI of 6°. At 6.60 nm wavelength with σ = 0.1 nm, the TIS is 22.2 % after seven reflections, approximately 3.8 times that at 13.50 nm. The TIS is 98.2 % after seven reflections with σ = 0.4 nm, so that surface roughness in BEUV mirrors is required to be under 0.4 nm, considering near-normal AOI mirrors. At 3.13 nm wavelength, the TIS is 67.2 % at 0.1 nm and 98.8 % at 0.2 nm after seven reflections, and 47.1 % with σ = 0.1 nm and 92.2 % with σ = 0.2 nm even in four reflections, requiring roughness to be under 0.2 nm.

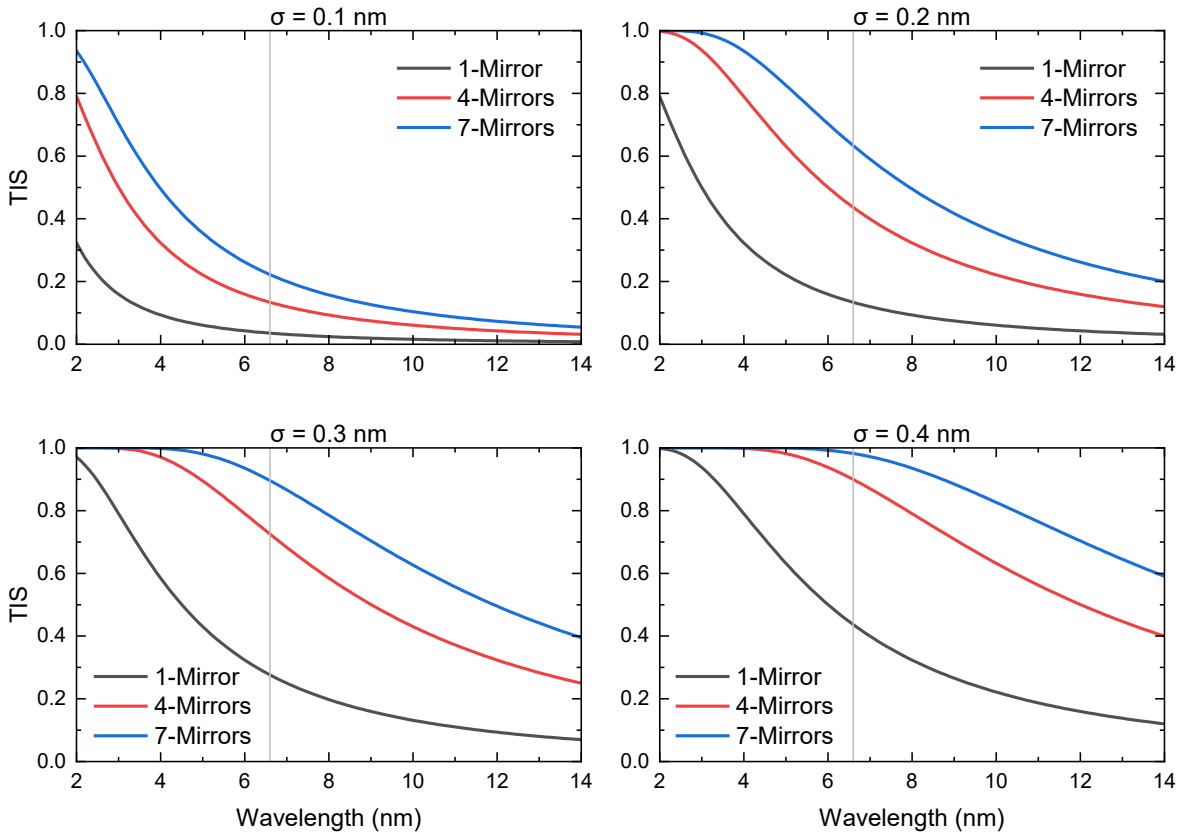


Fig. 1 Dependence of TIS on wavelength with the number of mirrors, assuming the roughness from 0.1 nm to 0.4 nm with AOI of 6°. The grey lines point to 6.6 nm wavelength.

Fig. 2-(a) shows the simulation of normalized reflectivity versus the roughness where Mo/Si = 2.81 nm/4.14 nm of 40 pairs at 13.50 nm, Mo_2N/B = 1.30/2.00 nm of 200 pairs at 6.60 nm, and Cr/Sc = 0.621 nm/0.952 nm of 500 pairs at 3.13 nm, based on the Parratt model including roughness [11,12]. The normalized reflectance is reduced to half when σ = 0.653 nm at 6.60 nm, and σ = 0.303 nm at 3.13 nm, whereas Mo/Si at 13.50 nm retains 0.79 of the reflectance even at σ = 1.0 nm. Fig. 2-(b) shows the background level (BGL) as the scattered light intensity, which is defined as the product of reflectance and TIS at 13.50 nm, 6.60 nm, and 3.13 nm. The BGL is suppressed at shorter wavelengths, but the peak positions shift to smaller σ due to the reflectance loss. The result clarifies that roughness requires to be under 0.5 nm in terms of the BGL for BEUV.

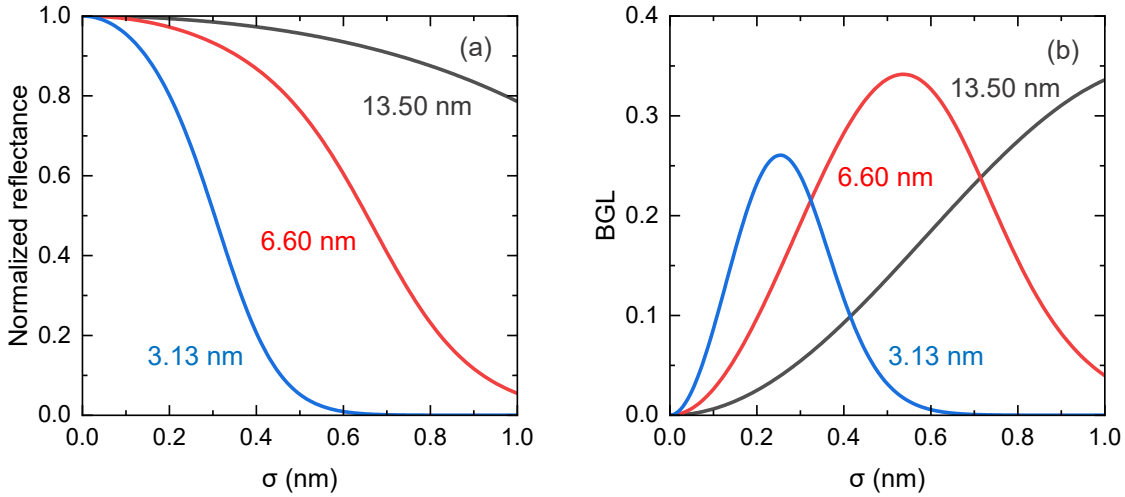


Fig. 2 (a) Normalized reflectivity versus roughness at 13.50, 6.60, and 3.13 nm, the AOIs are 6°, (b) Dependence of BGL on roughness at 13.50, 6.60, and 3.13 nm.

2.2 Surface growth

We investigate reactive PVD nitride growth as a route to minimizing surface roughness, and the relationship between reactive gas coverage as chemisorption and surface growth with roughness. Thin film growth has reported a link with the Kardar-Parisi-Zhang (KPZ) universality class, and the 1-dimensional (1D) KPZ equation is used to describe surface growth by Eq. (2) [13,14].

$$\partial_t h(x,t) = \nu\nabla^2 h + \frac{\Lambda}{2}(\nabla h)^2 + \eta(x,t) \tag{2}$$

where ν is a surface relaxation coefficient, Λ is a strength of nonlinear lateral growth term, $h \equiv h(x,t)$ is a height field with spatial coordinate x and time coordinate t, and $\eta(x,t)$ is a zero-mean

white Gaussian noise. The nonlinear term is discretized using the Lam-Shin form in Eq. (3), and the equation is integrated by a semi-implicit Fourier method [15].

$$(\nabla h)_i^2 \rightarrow \frac{(s^+)^2 + (s^-)^2 + s^+ s^-}{3\Delta x^2} \tag{3}$$

where $s^+ = h_{i+1} - h_i$, $s^- = h_i - h_{i-1}$ are the local slopes on the 1D chain. Complementing the KPZ surface growth scaling, the restricted solid-on-solid (RSOS) model can describe discrete step heights [16,17]. The surface is represented by integer heights h_i subject to the constraint as Eq. (4).

$$|h_{i+1} - h_i| \leq N \tag{4}$$

A site is chosen at random ($P = 1/L$ where L is the system size) and a unit deposition $h_i \rightarrow h_i + 1$ is accepted when the constraint of Eq. (4) remains satisfied. Varying the constraint from $N = 1$ to 3 changes the allowed step height but preserves the restricted solid-on-solid (RSOS) character of the surface. KPZ and RSOS models describe universal scaling during thin film growth, but they do not contain a kinetic parameter that can be related to deposition conditions such as reactive gas coverage. For chemisorption with controllable roughness evolution, we introduce a finite-mobility SOS model with the Ehrlich-Schwoebel (ES) barrier as Eq. (5) [18,19].

$$P_{acc} = \begin{cases} 0 & (\Delta h > 0) \\ 1 & (\Delta h = 0) \\ 1 - P_{ES} & (\Delta h < 0) \end{cases} \tag{5}$$

where P_{acc} is the acceptance probability for an attempted hop from site i to a neighboring site j, P_{ES} is the ES reflection probability that interpolates between smooth ($P_{ES} = 0$) and rough ($P_{ES} = 1.0$) growth kinetics, $\Delta h = h_j - h_i$. This reflection encodes the extra barrier for descending a step edge. The diffusion length is limited by a finite mobility, after each hop the walk continues with probability $q(\theta) = \Gamma_h(\theta)/(\Gamma_h(\theta) + \Gamma_t)$, where $\Gamma_h(\theta)$ is the hopping rate, and Γ_t is the rate at which the adatom loses mobility, so that $\left(1 - q(\theta)\right)^{-1}$ is an upper bound on the mean number of hops per adatom $\langle n_{hop} \rangle$. To quantify the roughening, we use the surface width $W(L,t)$, defined as Eq. (6).

$$W(L,t) = \langle \frac{1}{L} \sum_i (h_i - \langle h \rangle)^2 \rangle^{\frac{1}{2}} \tag{6}$$

In the Family-Vicsek picture, $W(L,t)$ grows as a power law of time before saturation and saturates with system size as Eq. (7) [20].

$$W(L,t) \sim t^{\beta} \ (t \ll t_{sat}) \rightarrow W_{sat} \sim L^{\alpha} \tag{7}$$

where β is the growth exponent, and α is the roughness exponent. The 1+1D Edwards-Wilkinson (EW) equation gives $\beta = 1/4$ and the KPZ equation gives $\beta = 1/3$ [21,22].

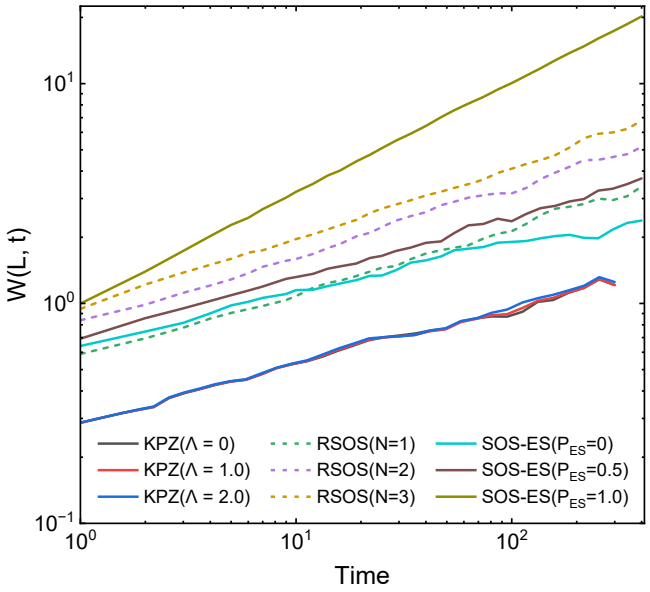


Fig. 3 Simulated kinetic roughening in 1+1D by the KPZ, the RSOS, and the finite-mobility SOS-ES models. The parameters are L = 512, ν = 1.0, Δt = 0.05 for the KPZ, RSOS, and q_0 = 0.9 for the SOS-ES.

Fig. 3 shows the time evolution of the surface width $W(t)$ as simulated roughness by the three models. In the KPZ model, $\Lambda = 0$ gives the EW limit, while $\Lambda > 0$ approaches the 1+1D KPZ value $\beta = 1/3$ with finite-time crossover effects remaining. The RSOS model with N = 1, 2, and 3 also yield near $\beta = 1/3$ (β changes from 0.30 to 0.33), so they do not provide a direct kinetic parameter for surface smoothing. In contrast, the finite-mobility SOS-ES models change β rising from about 0.2 at $P_{ES} = 0$ to 0.5 at $P_{ES} = 1.0$. The value at $P_{ES}(\theta) = 1.0$ is the effective slope of ES growth, and $P_{ES}(\theta) = 0$ is the smooth limit. Therefore, $P_{ES}(\theta)$ is the kinetic parameter among the three models that couples β to deposition conditions.

The chemisorbed nitrogen enters the growth through the barriers seen by a metal adatom, taken to be linear in the nitrogen occupancy of its local coordination shell: $E_{diff}(\theta) = E_{diff,0} - \varepsilon_D\theta$ within a terrace, and $E_{ES}(\theta) = E_{ES,0} - \varepsilon_S\theta$ for the excess barrier for descending a step. As $E_{ES}(\theta)$ is an excess over $E_{diff}(\theta)$, the couplings ε_S and ε_D are independent and ε_D may take either sign, so that chemisorbed nitrogen may act as a surfactant or as a poison for terrace diffusion. The diffusivity follows $E_{diff}(\theta)$ as Eq. (8) [23,24].

$$D_s(\theta) = D_s(0)\exp[\varepsilon_D\theta/k_BT] \tag{8}$$

where $D_s(0)$ is the diffusivity at zero coverage. We use $E_{ES,0}/k_BT = 2.5$, $\varepsilon_S/k_BT = 2.5$, $E_{diff,0}/k_BT = 1.5$, ε_D/k_BT = +1.0, 0, and -1.0, and $\Gamma_h(\theta) \propto D_s(\theta)$ with $\Gamma_h(0)/\Gamma_t = 9$, which give $q(0) = 0.90$

and $P_{ES}(0) = 0.92$. The diffusion length $l_D(\theta) = \left(1 - q(\theta)\right)^{-1/2}$ is evaluated at the deposition sites. The coverage follows from the balance between dissociative supply, associative desorption, and burial in the surface reaction, given by the Langmuir-Hinshelwood (LH) model as Eq. (9) [25,26].

$$\partial_t \theta = 2k_a p_N (1-\theta)^2 - 2k_d \theta^2 - k_r \theta_M \theta \tag{9}$$

where k_a, k_d, and k_r are the adsorption, desorption, and reaction rate constants, p_N is the partial gas pressure, and θ_M is the fraction of unreacted sites. The steady state θ_{SS} ($0 \le \theta_{SS} < 1$) follows from the steady-state condition of Eq. (9) as a mean-field relation, using the simulated coverage. With $1 - P_{ES} = \exp[-E_{ES}(\theta)/k_B T]$ of Eq. (5), the ES barrier enters as the length of Eq. (10).

$$l_{ES}(\theta) = P_{ES}(\theta)/\left(1 - P_{ES}(\theta)\right), \qquad \Omega(\theta) = l_{ES}(\theta)/l_D(\theta) \tag{10}$$

Fig. 4 shows the simulated roughness $\sigma = aW$ versus the coverage θ in 2+1D for single layers of 1, 10, and 100 nm, assuming $L^2 = 256 \times 256$ and $a = 0.25$ nm. The thickness corresponds to 4, 40, and 400 monolayers, which also serves as the growth time t. Over the simulated range $\theta = 0.065$-0.569 the roughness decreases by 37.9%, 59.6%, and 69.7%. $l_{ES}(\theta)$ falls from $9.75a$ to $2.44a$ and l_D rises only from $3.27a$ to $4.16a$, and Ω decreases from 2.99 to 0.59. As an adatom descends a step with probability $(1 + \Omega)^{-1}$, Ω governs the interlayer transport. The 100 nm roughness for $\varepsilon_D/k_B T = +1.0$, 0, and -1.0 collapses onto $\sigma \propto \Omega^{0.75}$ within 11%, whereas the $\varepsilon_S = 0$ control changes Ω by less than 25% and gives no reduction, so the smoothing follows ε_S, not the sign of ε_D. As θ_{SS} increases with the product $k_a p_N$, a coverage replaces the pressure as an independent variable.

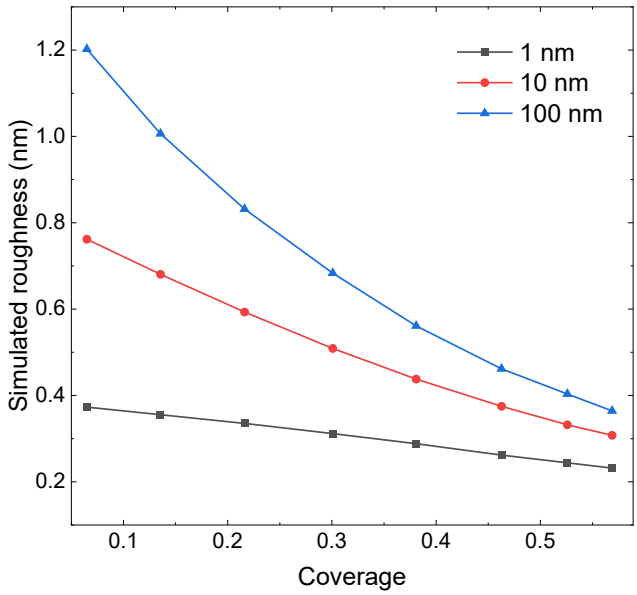


Fig. 4 Simulated roughness versus chemisorption coverage in 2+1D for single layers of 1 nm, 10 nm, and 100 nm.

3 Photomask

3.1 Optical constants

Fig. 5 shows the simulated optical constants at 6.60 nm wavelength based on Eqs. (11) and (12), using the CXRO database [27].

$$n = 1 - \frac{2\pi r_e \rho N_A}{k^2} \frac{\sum_j x_j f_{1j}}{\sum_j x_j A_r} \tag{11}$$

$$\kappa = \frac{2\pi r_e \rho N_A}{k^2} \frac{\sum_j x_j f_{2j}}{\sum_j x_j A_r} \tag{12}$$

where k is wavenumber, $r_e = 2.818\times10^{-15}$ m is the classical electron radius, $N_A = 6.022\times10^{23}$ mol^{-1} is the Avogadro number, ρ is the density, A_r is the atomic weight, f_{1j} and f_{2j} are the real and the imaginary parts of the atomic scattering factors, respectively. The density of the compound materials used for the calculation is referenced in Springer Materials [28].

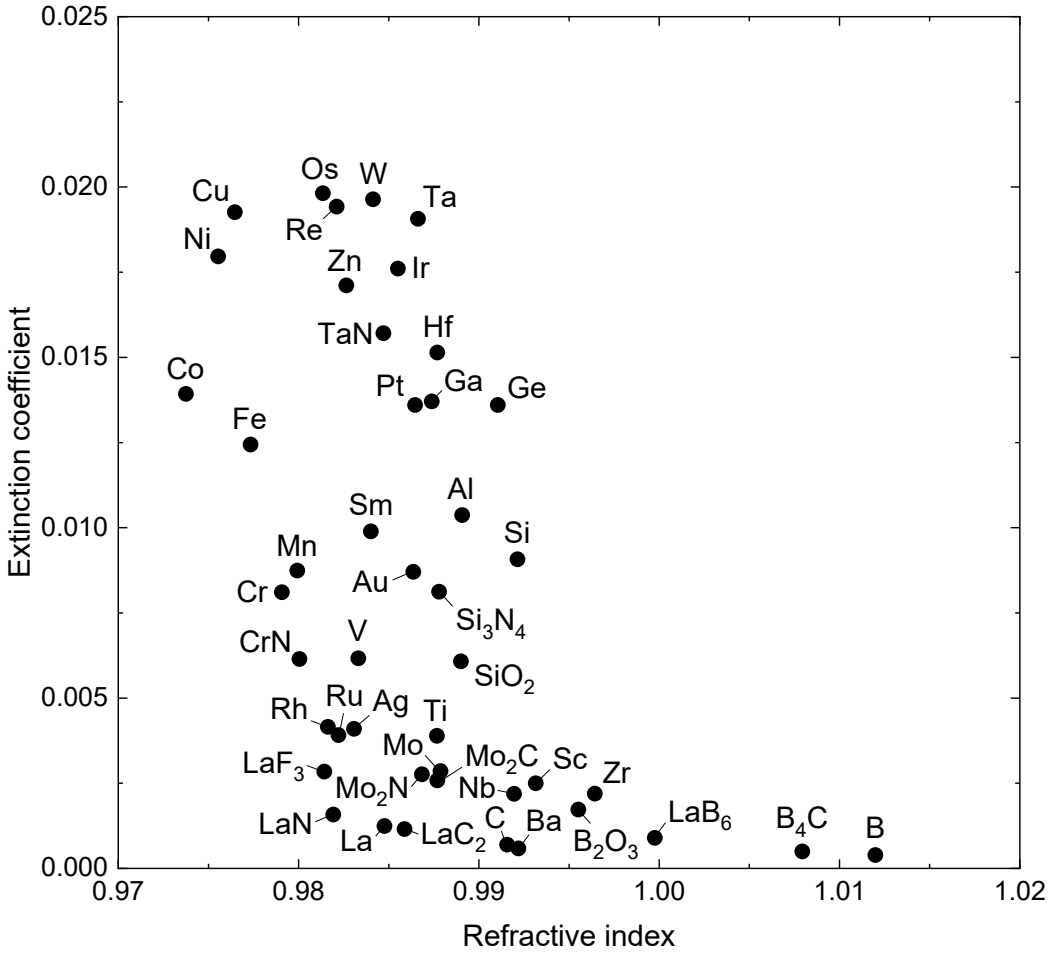
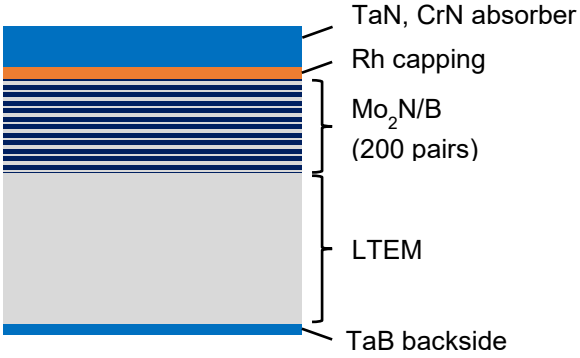


Fig. 5 Simulated optical constants at 6.60 nm wavelength.

(a)



(b)

Material	Refractive index	Extinction coefficient
TaN	0.984706	0.015707
CrN	0.980045	0.006142
Rh	0.981627	0.004152
Mo_2N	0.986841	0.002761
B	1.011994	0.000388

Fig. 6 (a) Schematic of proposed BEUV mask blank, (b) Simulated mask data at 6.60 nm wavelength.

3.2 Mask structure

We propose a BEUV mask blank as shown in Fig. 6-(a). The mask structure is composed of Mo_2N/B ML with 200 pairs, Rh capping layer, and absorber on a low thermal expansion substrate (LTEM) with TaB backside layer, assuming zero roughness at all interfaces. The Mo_2N/B ML is used as a BEUV mirror with an optimized thickness of 1.30 nm/2.00 nm at 6.60 nm wavelength with AOI of 6° [29]. Rh is selected as the capping material owing to its oxygen-based etching durability, and the thickness is 3.0 nm in this study [30,31]. As for BEUV absorber candidates, we compare TaN with CrN, and the optical constants of materials are shown in Fig. 6-(b) [27,28]. The TaB backside layer compensates for mask curvature and enables electrostatic chucking.

3.3 TaN and CrN absorbers

Figs. 7-(a) and (b) show the simulated reflectivity and phase difference based on the Parratt model, as the dependences of TaN and CrN absorber thickness at 6.6 nm wavelength and AOI of 6°. TaN provides a greater decrease in reflectivity than CrN, while CrN yields a greater phase shift for the same absorber thickness. At a phase difference of 135°, the thicknesses are 79.4 nm with 0.8 % for TaN and 62.6 nm with 17.1 % for CrN. TaN exhibits a significant decrease below 1 % at thicknesses above 70 nm, whereas CrN retains a reflectivity of 10.8 % at 83.0 nm thickness, and a phase difference of 180°. These results indicate that CrN is suitable for Att-PSMs because it provides sufficient margin against the reflectivity loss, and the sub-1 % reflectivity of TaN is usable for binary masks.

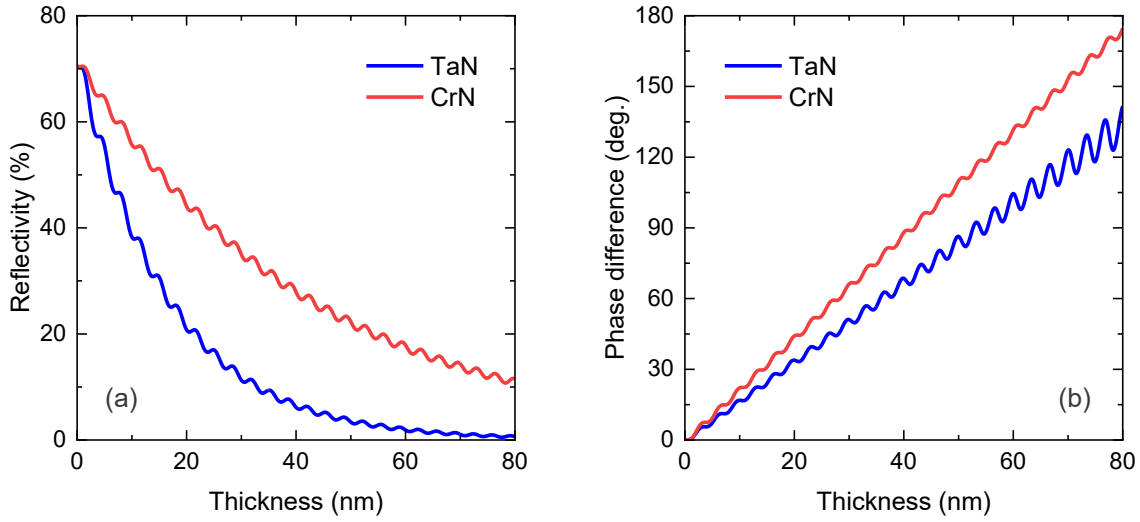


Fig. 7 (a) Simulated dependence of BEUV reflectivity on the absorber thickness, (b) Simulated dependence of phase difference on the absorber thickness.

The aerial image and the normalized image logarithmic slope (NILS) of the CrN-based Att-PSMs are formulated. Using the Abbe's method, each light source point $f_s \in [-\delta\,\mathrm{NA}/\lambda,\ +\delta\,\mathrm{NA}/\lambda]$, and the diffraction orders passing through the pupil ($|f_s + f_m| \le \mathrm{NA}/\lambda$, $f_m = m/P$) interfere coherently, and the partial image is summed incoherently in intensity over the source by Eq. (13).

$$I(x) = \frac{1}{N_s}\sum_{f_s}\left|\sum_{m:\ |f_s+f_m|\le \mathrm{NA}/\lambda} F_m\, e^{\,ik_0 W}\, e^{\,i2\pi f_m x}\right|^2 \tag{13}$$

The defocus z enters through the wavefront aberration in its exact, non-paraxial form $W = z(\cos\theta - 1)$, where $\sin\theta = \lambda(f_s + f_m)$. The complex reflectance of r_{abs} (absorber/line) and r_{ref} (space) with absorber thickness d_{abs} are obtained after phase correction as given by Eq. (14).

$$r^c_{\mathrm{abs}} = r_{\mathrm{abs}}\exp\left(-2i\,k_{z,\mathrm{vac}}\,d_{abs}\right), \qquad k_{z,\mathrm{vac}} = k_0\cos\theta_0 \tag{14}$$

The Fourier coefficients of a lattice $r(x)$ with period P and duty ratio d are given as Eq. (15).

$$F_0 = r^c_{\mathrm{abs}}\,d + r_{\mathrm{ref}}(1-d), \qquad F_{m\neq 0} = (r^c_{\mathrm{abs}} - r_{\mathrm{ref}})\frac{\sin(\pi m d)}{\pi m}\,e^{-i\pi m d} \tag{15}$$

The NILS is evaluated at the threshold $I_{\mathrm{th}} = (I_{\max} + I_{\min})/2$ and normalized by the line width ($w = P/2$ where P is the pitch), given as Eq. (16).

$$\mathrm{NILS} = w\left|\frac{d\ln I}{dx}\right| = \frac{P}{2}\left|\frac{1}{I}\frac{dI}{dx}\right| \tag{16}$$

A greater NILS denotes a sharper aerial image edge and larger exposure latitude at a given focus, and the NILS increases with higher NA.

Fig. 8-(a) shows the dependence of NILS on CrN thickness for 0.55 NA, 0.75 NA, and 0.85 NA. NILS rises with absorber thickness and saturates around 62.6 nm for the 0.55 NA, where CrN absorber gives a phase difference of 135°. The NILS values are 2.9 (0.55 NA), 4.2 (0.75 NA), and 4.6 (0.85 NA) when CrN absorber thickness is 80 nm. A higher NA gives a higher saturated NILS, and the relative gain from 0.55 NA to 0.85 NA is around 60 %. Fig. 8-(b) shows the aerial images for the three NAs when CrN = 62.6 nm. The DOF decreases with NA, the 0.55 NA remains broad and relatively flat across the entire scanned range, whereas the 0.85 NA curve forms a sharp peak.

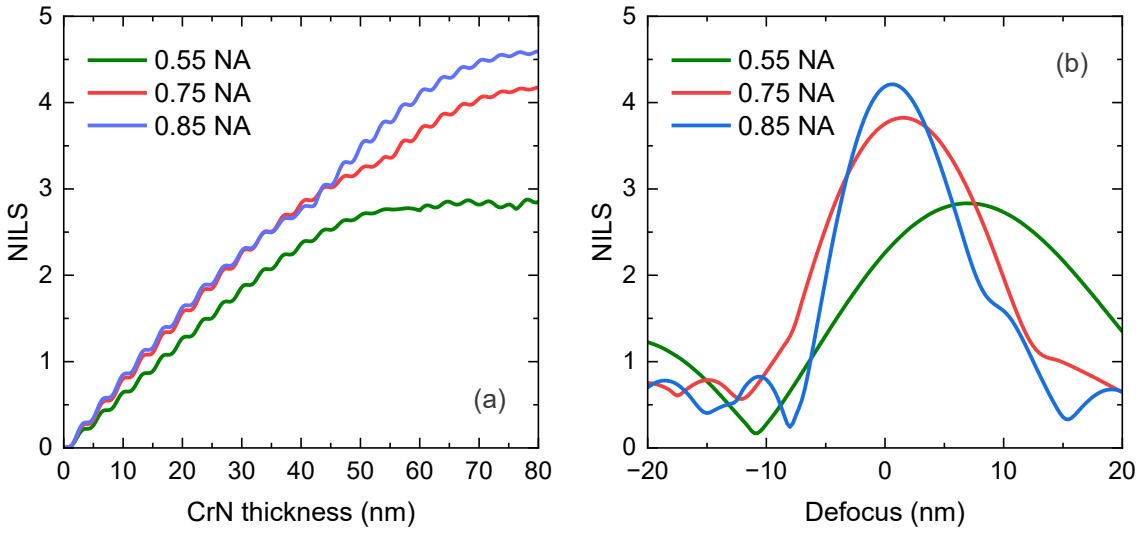


Fig. 8 (a) Simulated dependence of NILS on CrN thickness, (b) Simulated aerial images with CrN = 62.6 nm.

For M3D effect suppression, the sum of d_{abs} and Z_{eff} for a mask is required to be a smaller CD_{mask} on the mask as given by Eq. (17).

$$CD_{mask} = 2(d_{abs} + Z_{\text{eff}}) \tan\theta_i \tag{17}$$

Z_{eff} of Mo_2N/B ML is estimated from the AOI and the phase given by Eq. (18) [32].

$$\varphi \propto 2 \times Z_{\text{eff}} \times \frac{2\pi}{\lambda} \times (1 - \cos\theta_i) \cong Z_{\text{eff}} \times \frac{2\pi}{\lambda} \times {\theta_i}^2 \tag{18}$$

Fig. 9-(a) shows the simulated reflectivity at 6.6 nm in the Mo_2N/B thickness of 1.30 nm/2.00 nm, 1.10 nm/2.20 nm, 1.16 nm/2.15 nm optimized for AOI of 6°, 7°, and 8°. The AOI ranges of reflectivity over 70 % are 3.9°, 3.5°, 2.9°, respectively. Fig. 9-(b) shows the relationship between the Z_{eff} and AOI range calculated by the second polynomial approximation. The Z_{eff} in Mo_2N/B MLs are around 74 nm (1.30 nm/2.00 nm, 0-6°) and 74 nm (1.10 nm/2.20 nm, 0-7°), and 70 nm (1.16 nm/2.15 nm, 0-8°) which are 1.6 times larger than Mo/Si ML for EUV lithography [33].

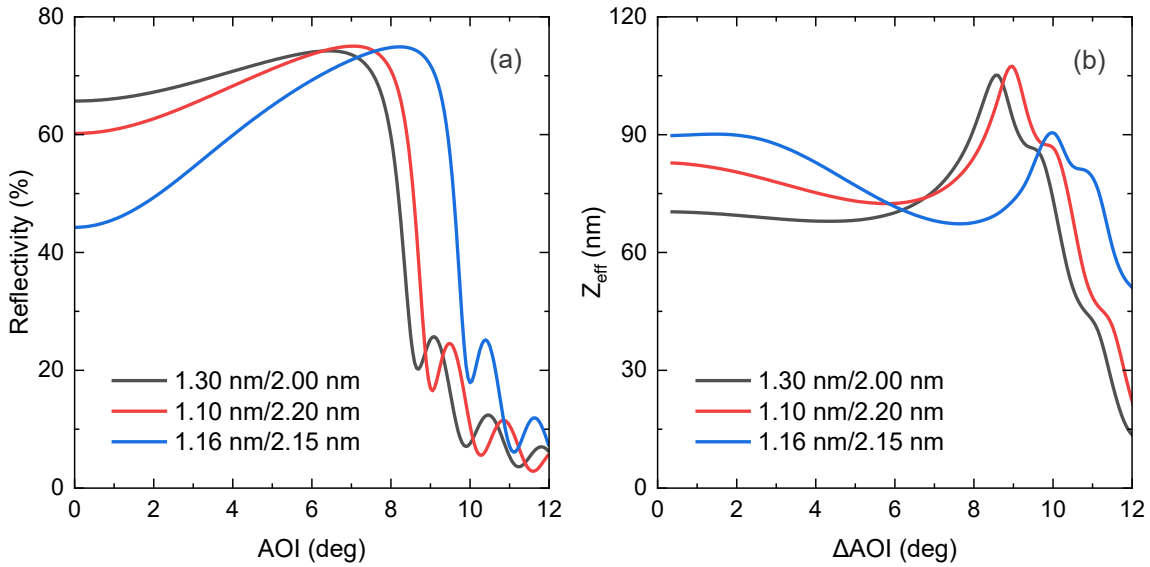


Fig. 9 (a) Simulated dependence of reflectivity at 6.60 nm on AOI in Mo_2N/B ML of 200 pairs, (b) The calculation of the Z_{eff} and the AOI range in Mo_2N/B ML of 200 pairs.

Table 2 summarizes the illumination-cone half-angles ($\alpha \parallel$, $\alpha \perp$) and common-plane phase variation ($\Delta\varphi_{cp} = \arg[r_{abs}/r_{ref}]$) for BEUV imaging with NA = 0.55, 0.75, and 0.85. We compare isomorphic 4x DM with anamorphic 4×/8× DM. At 0.55 NA, the anamorphic 4×/8× configuration keeps the chief-ray angle at object (CRAO) = 6° while halving the in-plane mask-side NA. For an anamorphic pupil, the cone half-angle is direction-dependent as $\alpha = \arcsin(NA/DM \parallel)$ in the plane of incidence $DM \parallel = 8$ and $\alpha = \arcsin(NA/DM \perp)$ in the cross-plane $DM \perp = 4$. At 0.55 NA, this reduces the in-plane full cone angle (2α) from 15.8° to 7.9° and the common-plane phase variation from 12.3° to 3.2°. The isomorphic 4x configuration at 0.55 NA is obscuration because $\alpha \parallel = 7.9°$ exceeds the 6° CRAO budget and causes incident/reflected pupil overlap. The 0.55 NA with 4×/8× DM and CrN of 62.6 nm is adopted as the high-NA BEUV architecture because the CD_{mask} for 0.75 NA and 0.85 NA are greater, assuming CrN = 62.6 nm and Z_{eff} at AOIs in Fig. 9-(b).

Table. 2 Specification of BEUV mask and lithography.

NA	DM	$\alpha \parallel$ (deg)	$\alpha \perp$ (deg)	$\Delta\varphi_{cp}$ (deg)	AOI (deg)	CD_{mask} (nm)	CD_{wafer} (nm)
0.55	4x	7.9	7.9	12.3	≥ 7.9	≥ 37.9	≥ 9.5
	4x/8x	3.9	7.9	3.2	≥ 3.9	≥ 18.6	≥ 2.3, ≥ 4.7
0.75	4x/8x	5.4	10.8	9.3	≥ 5.4	≥ 25.8	≥ 3.2, ≥ 6.5
0.85	4x/8x	6.1	12.3	12.3	≥ 6.1	≥ 28.3	≥ 3.5, ≥ 7.1

5 Discussion and Summary

In our ES-SOS model, the chemisorption coverage modifies the kinetic barriers for adatom diffusion and for the ES reflection at descending steps. Under this assumption, the simulated 2+1D growth exhibits suppressed kinetic roughening, which suggests an approach to reduce interface roughness in MLs such as Mo_2N/B. Our framework can be applied to various short-wavelength ML materials involving nitridation, such as Mo and La at 6.60 nm or Cr and Sc at 3.13 nm [29,34,35]. Coverage-controlled reactive sputtering is expected to narrow the roughness gap between MS and IBD for high-volume manufacturing. For BEUV photomasks, we evaluate the Att-PSM architecture using a Mo_2N/B ML, a Rh capping layer, and a CrN absorber. CrN gives a 135° phase shift at 62.6 nm thickness, where the NILS approaches saturation at 0.55 NA, while the Z_{eff} of 74 nm in the Mo_2N/B ML requires the anamorphic 4x/8x DM to keep CD_{mask} small. We show that 0.55 NA with 4x/8x DM at an AOI of 6° is promising for high-NA BEUV lithography.

Disclosures

The authors declare that there are no financial interests, commercial affiliations, or other potential conflicts of interest that could have influenced the objectivity of this research or the writing of this paper.

Code, Data, and Materials Availability

The data that supports the findings of this study are available from the corresponding authors on request and https://github.com/nhayase/JM3-260022P-1.

Acknowledgments

This work was partially supported by Hyogo Earthquake Memorial 21st Century Research Institute, Hyogo Foundation for Science and Technology, Tanaka Kikinzoku Memorial Foundation, Takahashi Industrial and Economic Research Foundation, and Foundation of Kinoshita Memorial Enterprise.

References

1. N. Hayase, T. Harada, "Beyond EUV binary and phase shift masks simulation," *Proc. SPIE* **13177**, 315-322 (2024).

2. I. Lee, J. H. Franke, V. Philipsen, K. Ronse, S. De Gendt, E. Hendrickx, "Study on next-generation EUV lithography technology: hyper NA, the highest potential for practical implementation," *ACS Appl. Mater. Interfaces* **17**(33), 47719-47735 (2025).
3. T. Liang, H. Miyai, S. Sayan, M. Mizoguchi, K. Gondaira, M. Nishizawa, T. Suzuki, T. Todoroki, Y. Li, F. Abboud, "Actinic mask inspection for the era of high-numerical aperture extreme ultraviolet lithography," *J. Micro/Nanopatterning Mater. Metrol.* **24**(1), 011006 (2025).
4. Y. Chen, D. Hahner, M. Trubetskov, S. Schrameyer, W. Sakiew, K. Starke, V. Pervak, "Comparison of magnetron sputtering and ion beam sputtering on dispersive mirrors," *Appl. Phys. B* **126**(5), 82 (2020).
5. K. Rook, A. Checco, P. Turner, A. A. Kulkarni, K. Yamamoto, M. H. Lee, "Comparison of deposition techniques for Mo/Si reflective multilayers for EUV mask blanks," *Proc. SPIE* **11854**, 115-120 (2021).
6. V. Bakshi, "Blue-X: exploring advanced optical projection lithography below 13.5 nm," *Proc. SPIE* **13979** (2026).
7. S. Sherwin, M. Hettermann, D. Houser, P. Naulleau, "Understanding and measuring EUV mask 3D effects," *J. Micro/Nanopatterning Mater. Metrol.* **23**(4), 041407 (2024).
8. A. Erdmann, H. Mesilhy, P. Evanschitzky "Attenuated phase shift masks: a wild card resolution enhancement for extreme ultraviolet lithography?" *J. Micro/Nanopatterning Mater. Metrol.* **21**(2), 020901 (2022).
9. E. L. Church, P. Z. Takacs, "Handbook of Optics, Vol. 1, Chapter 7 Surface Scattering," *McGraw-Hill* (1995).
10. J. E. Harvey, S. Schröder, N. Choi, A. Duparré, "Total integrated scatter from surfaces with arbitrary roughness, correlation widths, and incident angles," *Opt. Eng.* **51**(1), 013402 (2012).
11. L. G. Parratt, "Surface studies of solids by total reflection of X-rays," *Phys. Rev.* **95**(2), 359 (1954).
12. D. K. G. De Boer, "X-ray reflection and transmission by rough surfaces," *Phys. Rev. B* **51**(8), 5297 (1995).
13. R. A. L. Almeida, S. O. Ferreira, T. J. Oliveira, F. A. Reis, "Universal fluctuations in the growth of semiconductor thin films," *Phys. Rev. B* **89**(4), 045309 (2014).
14. M. Kardar, G. Parisi, Y. C. Zhang, "Dynamic scaling of growing interfaces," *Phys. Rev. Lett.* **56**(9), 889 (1986).
15. Chi-Hang Lam, F. G. Shin, "Anomaly in numerical integrations of the Kardar-Parisi-Zhang equation," *Phys. Rev. E* **57**(6), 6506 (1998).
16. J. M. Kim, J. M. Kosterlitz, "Growth in a restricted solid-on-solid model," *Phys. Rev. Lett.* **62**, 2289 (1989).

17. M. Siegert, M. Plischke, “Solid-on-solid models of molecular-beam epitaxy,” *Phys. Rev. E* **50**(2), 917 (1994).
18. G. Ehrlich, F. G. Hudda, “Atomic View of Surface Self-Diffusion: Tungsten on Tungsten,” *J. Chem. Phys.* **44**, 1039–1049 (1966).
19. R. L. Schwoebel, E. J. Shipsey, “Step Motion on Crystal Surfaces,” *J. Appl. Phys.* **37**(10), 3682–3686 (1966).
20. F. Family, T. Vicsek, “Scaling of the active zone in the Eden process on percolation networks and the ballistic deposition model,” *J. Phys. A: Math. Gen.* **18** L75 (1985).
21. J. Krug, “Origins of scale invariance in growth processes,” *Adv. Phys.* **46**(2), 139–282 (1997).
22. S. F. Edwards, D. R. Wilkinson, “The Surface Statistics of a Granular Aggregate,” *Proc. R. Soc. Lond. A* **381**, 17 (1982).
23. M. Copel, M. C. Reuter, E. Kaxiras, R. M. Tromp, "Surfactants in epitaxial growth," *Phys. Rev. Lett.* **63**, 632–635 (1989).
24. J. Villain, “Continuum models of crystal growth from atomic beams with and without desorption,” *J. Phys. I* **1**, 19–42 (1991).
25. O. A. Hougen, K. M. Watson, “General principles,” *Ind. Eng. Chem.* **35**(5), 529-541 (1943).
26. S. Berg, T. Nyberg, "Fundamental understanding and modeling of reactive sputtering processes," *Thin Solid Films* **476**(2), 215–230 (2005).
27. B. L. Henke, E. M. Gullikson, J. C. Davis, “X-ray interactions: photoabsorption, scattering, transmission, and reflection at E= 50-30,000 eV, Z= 1-92,” *Atomic data and nuclear data tables* **54**(2), 181-342 (1993).
28. Springer Materials, https://materials.springer.com
29. N. Hayase, M. Yoshimura, S. Suzuki, S. Yamakawa, T. Harada, “Mo-based multilayer for beyond EUV lithography,” *Proc. SPIE* **13983** (2026).
30. M. Singh, J. J. M. Braat, “Capping layers for extreme-ultraviolet multilayer interference coatings,” *Opt. Lett.* **26**(5), 259 (2001).
31. J. Gustafson, A. Mikkelsen, M. Borg, E. Lundgren, L. Köhler, G. Kresse, M. Schmid, P. Varga, J. Yuhara, X. Torrelles, C. Quirós, J. N. Andersen, “Self-Limited Growth of a Thin Oxide Layer on Rh(111),” *Phys. Rev. Lett.* **92**, 126102 (2004).
32. M. F. Bal, M. Singh, J. J. M. Braat “Optimization of multilayer reflectors for extreme ultraviolet lithography,” *J. Micro/Nanolithogr., MEMS, MOEMS* **3**(4), 537-544 (2004).
33. O. Wood II, K. Wong, V. Parks, P. Kearney, J. Meyer-Ilse, V. Luong, V. Philipsen, M. Faheem, Y. Liang, A. Kumar, E. Chen, C. Bennett, B. Fu, M. Gribelyuk, W. Zhao, P. Mangat, P. Van der Heide,

"Improved Ru/Si multilayer reflective coatings for advanced extreme-ultraviolet lithography photomasks," *Proc. SPIE* **9776**, 364-373 (2016).

34. D. S. Kuznetsov, A. E. Yakshin, J. M. Sturm, R. van de Kruijs, E. Louis, F. Bijkerk, "High-reflectance La/B-based multilayer mirror for 6. x nm wavelength," *Opt. Lett.* **40**(16), 3778-3781 (2015).
35. F. Delmotte, E. Meltchakov, A. Sokolov, P. Mercère, B. Capitanio, E. Gullikson, "At wavelength metrology of high-reflectance multilayer mirror in the water window," *J. Appl. Phys.* **139**(1), 013107 (2026).

Biographies and photographs for the other authors are not available.